ACS NANO
Cite This: ACS Nano 2018, 12, 1285−1295
www.acsnano.org

ARTICLE

Structural Changes as a Function of Thickness in $[(SnSe)_{1+\delta}]_mTiSe_2$ Heterostructures

Danielle M. Hamann,[†] Alexander C. Lygo,[†] Marco Esters,[†] Devin R. Merrill,[†] Jeffrey Ditto,[†] Duncan R. Sutherland,[†] Sage R. Bauers,[†,§] and David C. Johnson*[,†]

[†]Department of Chemistry, Materials Science Institute, University of Oregon, Eugene, Oregon 97403, United States
[§]National Renewable Energy Laboratory, Golden, Colorado 80401, United States

Supporting Information

ABSTRACT: Single- and few-layer metal chalcogenide compounds are of significant interest due to structural changes and emergent electronic properties on reducing dimensionality from three to two dimensions. To explore dimensionality effects in SnSe, a series of $[(SnSe)_{1+\delta}]_mTiSe_2$ intergrowth structures with increasing SnSe layer thickness (m = 1−4) were prepared from designed thin-film precursors. In-plane diffraction patterns indicated that significant structural changes occurred in the basal plane of the SnSe constituent as m is increased. Scanning transmission electron microscopy cross-sectional images of the m = 1 compound indicate long-range coherence between layers, whereas the $m \geq 2$ compounds show extensive rotational disorder between the constituent layers. For $m \geq 2$, the images of the SnSe constituent contain a variety of stacking sequences of SnSe bilayers. Density functional theory calculations suggest that the formation energy is similar for several different SnSe stacking sequences. The compounds show unexpected transport properties as m is increased, including the first p-type behavior observed in $(MSe)_m(TiSe_2)_n$ compounds. The resistivity of the $m \geq 2$ compounds is larger than for m = 1, with m = 2 being the largest. At room temperature, the Hall coefficient is positive for m = 1 and negative for m = 2−4. The Hall coefficient of the m = 2 compound changes sign as temperature is decreased. The room-temperature Seebeck coefficient, however, switches from negative to positive at m = 3. These properties are incompatible with single band transport indicating that the compounds are not simple composites.

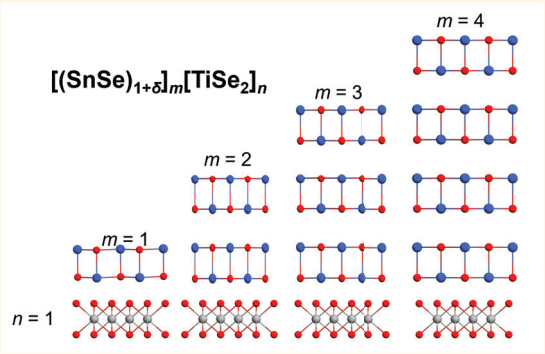

KEYWORDS: *heterostructures, layered compound, structural distortion, kinetic products, low-dimensional materials, tin selenide*

Two-dimensional (2D) materials continue to attract increasing attention as researchers discover emergent electronic properties in monolayers and heterostructures.[1−5] For example, transitions from an indirect to a direct band gap have been discovered in semiconducting TX_2 (T = Mo, W; X = S, Se) compounds on going from a bilayer to a monolayer as interactions with the neighboring TX_2 layer are eliminated.[6−8] The properties of single layers are impacted by interactions with the substrate and/or adjacent layers, with the overlap of states and the band offsets suggested as being important factors.[9−12] This has led to the concept of 2D layers acting as building blocks that can be stacked in specific sequences, yielding heterostructures with desired properties.[13] Understanding how layers interact with one another to yield emergent properties is critical to enable materials design for specific applications and is a current focus of the materials community.

Less well investigated are structural modifications associated with changes in electronic structure as these heterostructures are created. There are several reasons for this, including challenges in obtaining direct structural information on ultrathin layers, lack of structural information from common analytical techniques used to confirm layering, and the initial systems investigated being rigid layers with van der Waals gaps on both sides in the bulk (graphene, HBN, transition metal dichalcogenides, *etc.*) where only small distortions might be expected. Since there are a limited number of rigid structures with a narrow subset of properties, researchers have begun to explore 2D layers of compounds with 3D structures. Structural changes are more pronounced in 2D layers of materials with bulk 3D structures as the layers distort to stabilize dangling bonds at the interfaces. For example, bilayers of bulk rock salt structured constituents between dichalcogenide layers distort significantly, with the cations moving as much as 0.2 Å toward

Received: October 23, 2017
Accepted: January 31, 2018
Published: January 31, 2018

DOI: 10.1021/acsnano.7b07506
ACS Nano 2018, 12, 1285−1295

the anion layers in the dichalcogenide.[14,15] As the thickness of rock salt structured layers is increased, the distortions evolve toward a bulk structure with a surface distortion at the interface.[14,16] These structural distortions reflect changes in the free energy landscape as the ratio of atoms at the interface relative to those interior decreases. The properties of these heterostructures have been observed to systematically change as layer thicknesses are varied, reflecting the interactions between the layers.[17−19] Understanding how structural distortions in 3D materials change as their thickness approaches the 2D limit and how these distortions impact their properties is necessary to design heterostructures with specific properties.

This paper investigates structural transitions in SnSe as a function of layer thickness in heterostructures also containing a $TiSe_2$ monolayer. The naming convention for these structures is $[(SnSe)_{1+\delta}]_m[TiSe_2]_1$ where m is the number of SnSe bilayers between the single layers of $TiSe_2$ and the $1+\delta$ term accounts for the difference in basal plane area between the two constituents. SnSe was chosen because bulk SnSe undergoes a structural transition from the room-temperature phase, α-SnSe (GeS structure, *pcmn*), to the high-temperature β-SnSe (TlI structure, *Cmcm*) structure.[20] Von Schnering and co-workers investigated this phase transition in detail as a model system to test Landau theory predictions about symmetry-breaking changes in solids.[21−23] They found that the distortion is second order, with the Sn and Se x-coordinates changing continuously between the distorted α-SnSe structure and the undistorted β-SnSe structure. This investigation probes how the SnSe structure is impacted by layer thickness when stacked in a heterostructure. SnSe has been incorporated into heterostructures with several TX_2 layers, where T = V, Nb, Mo, and Ta.[19,24−27] In this work $TiSe_2$ was chosen as a second constituent because $(SnSe)_{1.21}(TiSe_2)$ prepared from modulated reactants is unique in having long-range order, where the SnSe structure distorts to obtain an epitaxial relationship with $TiSe_2$.[28] Increasing the thickness of the SnSe constituent will create a competition between the surface free energy, which favors the formation of an epitaxial relationship, and the bulk free energy, which would be expected to result in a bulk structure for a sufficiently thick SnSe layer. In-plane X-ray diffraction (XRD) revealed that as the thickness of the SnSe layer is increased, the structure distorts significantly from a rectangular in-plane unit cell when m = 1 to a different rectangular unit cell that is related to the bulk α-SnSe orthorhombic structure for m = 4. High-angle annular dark field scanning transmission electron microscopy (HAADF-STEM) images reveal a variety of stacking sequences of the SnSe bilayers as the SnSe thickness increases. Density functional theory (DFT) calculations suggest that the structural changes cannot be explained by isolated SnSe layers, but are impacted by interactions between the constituent layers. Electrical transport measurements reveal independent changes in the signs of the Hall coefficient and Seebeck coefficient with increasing m and changes in temperature, reflecting the complex interactions between the layers. This is the first time p-type behavior has been observed in $(MSe)_m(TiSe_2)_n$ compounds. The interplay between constituent layers provides an opportunity to customize desired properties by adjusting the identity, thickness, and/or stacking sequence of 2D layers.

RESULTS AND DISCUSSION

The modulated elemental reactants (MER) approach was used to prepare the targeted $[(SnSe)_{1+\delta}]_mTiSe_2$ ferecrystalline compounds (turbostratically disordered polymorphs of misfit layer compounds).[29,30] The deposition parameters required to prepare layered amorphous precursors that closely resemble the targeted structure in both local composition and layer thickness were determined using an iterative approach. This involved preparing a series of precursors of the sequence $\{1 \times [TiSe] + m \times [SnSe]\}$ with varying m and n values, measuring their compositions *via* electron probe microanalysis (EPMA), measuring the thickness of the repeating amorphous sequence *via* X-ray reflectivity (XRR), and interpolating to obtain desired compositions and thicknesses as described previously.[24] Once the deposition was calibrated, precursors for each of the targeted $[(SnSe)_{1+\delta}]_mTiSe_2$ compounds were prepared by depositing the $\{[TiSe] + m \times [SnSe]\}$ sequence the required number of times to obtain the desired total thickness. An annealing study was conducted to determine optimum annealing temperatures and times to transform the designed precursors into the targeted compounds. The line widths and intensities of the reflections in specular XRD were used to assess the quality of the samples. A temperature of 350 °C for 30 min was selected as the optimum annealing conditions to crystallize the desired products. These conditions were the same as those used previously to prepare $(SnSe)_{1.2}TiSe_2$.[31]

The specular XRD patterns of the annealed precursors are shown in Figure 1. Only (00*l*) reflections are observed in the

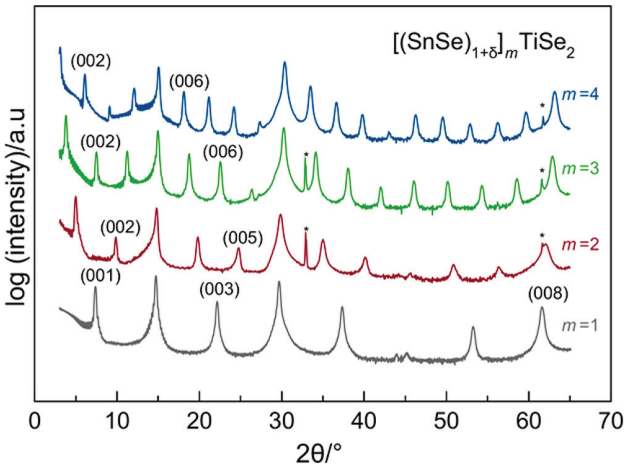

Figure 1. Specular X-ray diffraction scans of $[(SnSe)_{1+\delta}]_mTiSe_2$ compounds (m = 1−4). The intensity is plotted on a log scale to enhance weak reflections. Miller indices are provided for select reflections, and asterisks indicate reflections from the Si substrate.

patterns, indicating that the *c*-axis of the targeted compounds is perpendicular to the Si substrate. All reflections are narrow and sharp and can be indexed to a single family of planes, suggesting that a single repeating structure is formed. The calculated *c*-axis lattice parameters for the products are summarized in Table 1. As the number of SnSe bilayers deposited in the precursor

Table 1. Lattice Parameters and Misfit Parameters for $[(SnSe)_{1+\delta}]_mTiSe_2$ Compounds

m	SnSe a (Å)	SnSe b (Å)	$TiSe_2$ a (Å)	$1+\delta$	c (Å)
1	6.1036(6)	5.9787(4)	3.56(1)	1.203(9)	12.04(1)
2	4.2320(7)	4.2887(7)	3.60(5)	1.24(7)	17.84(1)
3	4.2487(4)	4.3126(4)	3.56(1)	1.198(7)	23.64(1)
4	4.2401(4)	4.3196(5)	3.56(1)	1.196(8)	29.42(2)

DOI: 10.1021/acsnano.7b07506
ACS Nano 2018, 12, 1285−1295

increases, there is a systematic increase in the *c*-axis lattice parameter of 5.79(1) Å per bilayer of SnSe in $[(SnSe)_{1+\delta}]_mTiSe_2$. This result is consistent with the 5.77(5) and 5.806(2) Å increase in the *c*-axis lattice parameter per SnSe bilayer reported for $[(SnSe)_{1+\delta}]_m[NbSe_2]_n$- and $[(SnSe)_{1+\delta}]_m[MoSe_2]_n$-based compounds, respectively.[17,32] Extrapolating this relationship to $m = 0$, the thickness of the single $TiSe_2$ layer is 6.25(3) Å in each compound, which is thicker than the *c*-axis lattice parameter of bulk $TiSe_2$ (6.008 Å)[33] and the thickness per $TiSe_2$ layer in $(PbSe)_{1+\delta}[TiSe_2]_n$ (6.03–6.04 Å) obtained from the change in *c*-axis lattice parameter as *n* is varied.[18,34,35] The larger value reflects the different species interacting across the van der Waals interface. A single $TiSe_2$ layer has two $TiSe_2$–SnSe interfaces that are mismatched and hence cannot nest together. The extrapolated $TiSe_2$ thickness in the $[(SnSe)_{1+\delta}]_mTiSe_2$ compounds also reflects other interactions between the constituents, such as charge transfer.

In-plane diffraction patterns were collected to characterize the basal plane structures of the constituent layers and are shown in Figure 2a. All observed reflections can be indexed to either a hexagonal unit cell for $TiSe_2$ or a rectangular unit cell for SnSe, except for reflections marked with a cross. The extra reflections at 48° in the $m = 2$–4 patterns and at 90° for $m = 2$, 4 patterns are consistent with (110) and (300) $SnSe_2$ reflections and are likely the result of a slight excess of Sn and Se in the precursor. The in-plane lattice parameters for each constituent were refined using a full pattern Le Bail[36] fit and are summarized in Table 1. The results of the fits can be found in Figures S1–S4 in the Supporting Information. The larger errors in the $TiSe_2$ lattice parameters relative to the SnSe lattice parameters result from overlapping reflections, with only the (110) reflection of $TiSe_2$ being distinct from reflections of SnSe. The hexagonal $TiSe_2$ reflections yield *a*-axis lattice parameters of 3.56(1) Å, except for the $m = 2$ compound, which has an *a*-axis lattice parameter of 3.60(5) Å. The larger error for the $m = 2$ compound is a consequence of the overlap of the $TiSe_2$ (110) reflection with the (110) $SnSe_2$ reflection (Figure 2a). These *a*-axis lattice parameters are within error of each other and are consistent with those previously reported for other ferecrystals containing $TiSe_2$ layers and the binary $TiSe_2$ compound.[18,34,35,37−39] This suggests that the in-plane structure of $TiSe_2$ is independent of the SnSe layer thickness.

Surprisingly, the in-plane diffraction patterns for SnSe change considerably as *m* increases. Splitting, merging, and shifting of reflections indicate that the symmetry and lattice parameters change substantially as *m* is varied. Figure 2b contains an expanded view of a high-angle region containing several reflections to highlight the changes in the in-plane unit cell of SnSe as *m* is increased. The $m = 1$ compound has two reflections occurring at 60.6° and 62.2° that can be indexed as the (400) and (040) reflections in a distorted rock salt structure. In contrast, the $m = 4$ compound has a single reflection at 61.3° that can be indexed as a (220) reflection of a rectangular basal plane unit cell, which is consistent with either a distorted α-SnSe or β-SnSe structure. The shifts in reflection positions for the $m = 1$ and $m = 4$ patterns require different unit cells and indexing. This is most visible at higher angles (Figure 2c). At higher angles between 85° and 110°, the patterns for the $m = 2$ and $m = 3$ compounds have reflections at the same angles as for $m = 4$. Because of the similarity in the diffraction patterns, the $m = 2$ and 3 compounds can be indexed in the same manner as the $m = 4$ compounds. When looking at the reflection around 69°, the $m = 1$ and 4 compounds are clearly

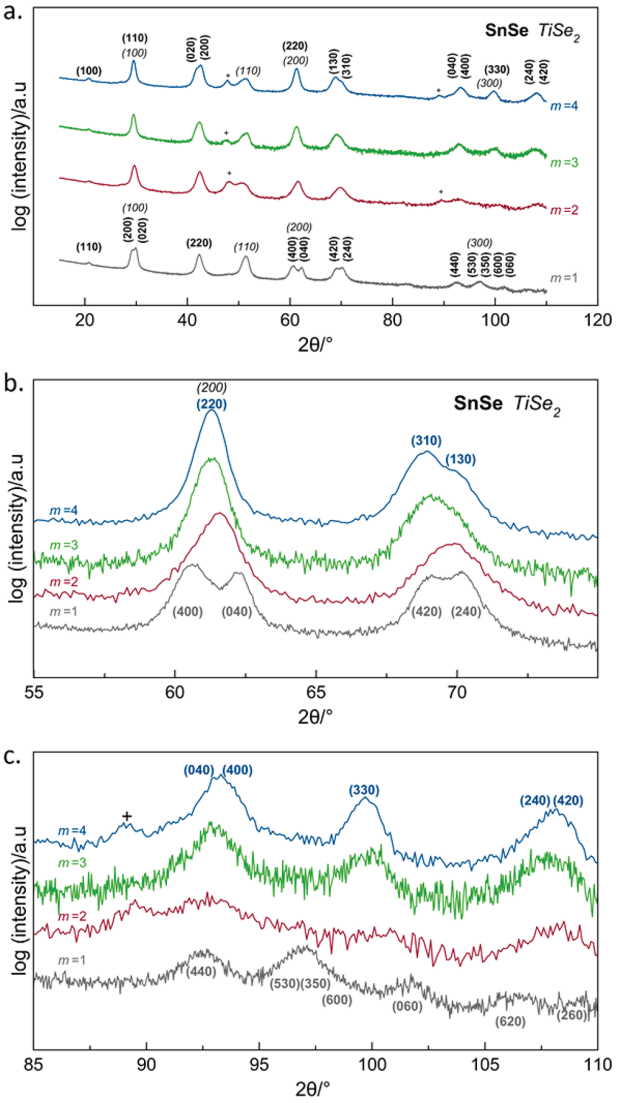

Figure 2. (a) In-plane diffraction pattern of the $[(SnSe)_{1+\delta}]_mTiSe_2$ compounds where $1 \leq m \leq 4$. The reflections are indexed to either SnSe or $TiSe_2$, with a single impurity peak being indexed to $SnSe_2$ (denoted with a + symbol). (b) Expansion of the high-angle region emphasizing the change in the SnSe reflections at approximately 61° and 69° that occurs as *m* is increased from 1 to 4. (c) Expansion of a higher angle region that highlights the reflection differences between the $m = 1$ and $m \geq 2$ in-plane diffraction patterns.

rectangular, as indicated by the splitting of the peak. Although no splitting is observed for the $m = 2$ and 3 compounds, a line width broadening of the $h \neq k$ reflections compared to the $h = k$ reflections is present, suggesting the basal plane is rectangular for these compounds as well.

Changes in the structure of SnSe layers with thickness have previously been reported for both misfit layer compounds and ferecrystals. In misfit layer compounds, bilayers of SnSe adopt a distorted NaCl structure, where the Sn atoms move toward the dichalcogenide and the Se atoms are displaced away from it.[35] There are additional distortions due to the structures adopting a common in-plane lattice parameter in one direction. In ferecrystals, the Sn atoms also move toward the dichalcogenide and the Se atoms are displaced away from it. However, the in-

DOI: 10.1021/acsnano.7b07506
ACS Nano 2018, 12, 1285–1295

plane structure of the SnSe layer changes with thickness, while the dichalcogenide unit cell does not vary. In compounds with a single SnSe bilayer ($m = 1$), the basal plane unit cell of the SnSe is typically square or very close to square. Thicker SnSe layers have rectangular in-plane unit cells that approach the bulk low-temperature structure (α-SnSe) as m increases. This trend is observed for the $m \geq 2$ compounds reported herein, with $m = 1$ deviating significantly. As reported previously, however, $(SnSe)_{1.21}TiSe_2$ is the only example of a compound that forms large domains with ordering between the constituent layers when prepared *via* the low-temperature self-assembly of a layered precursor. It is thought that the epitaxial relationship results from a coincidental lattice match between SnSe and $TiSe_2$.[28] The $m = n = 1$ compound is best described as a misfit layer compound with a large number of rotational defects present. The significant changes in structure as m is increased reflect the decreased importance of surface free energy as the thickness of the SnSe layer is increased.

In contrast to the $m = 1$ compound, the SnSe layer in the $m = 4$ compound has an in-plane structure that is closest to the bulk, reflecting a decrease in the surface to volume ratio of the SnSe layer. The structure is indexed to a rectangular in-plane unit cell, and the a and b lattice parameters are similar to those measured for the bulk at a temperature of approximately 700 K as it transforms between the α-SnSe and β-SnSe structures. Similar changes in the basal plane structure as a function of m have been previously observed in the $[(SnSe)_{1+\delta}]_m[TaSe_2]_n$ and $[(SnSe)_{1+\delta}]_m[MoSe_2]_n$ systems[24,25] The lattice parameters for the compounds with $m = 2$ and 3 are similar to the in-plane lattice parameters of either the α-SnSe structure at 800 K or the β-SnSe structure at 825 K. The lattice parameters, however, are smaller than those reported for β-SnSe. If the $m \geq 2$ compounds possessed either the GeS or TlI SnSe bulk structure, the (100) reflection would be extinct. Its presence indicates the existence of small distortions that change the atomic positions within the *ab*-plane. The large difference between the lattice parameters for $m = 1$ and $m \geq 2$ results from redefining the unit cell from a face-centered unit cell to a primitive unit cell to be consistent with von Schnering and co-workers.[21−23] The relationship between the two different unit cells and the shift in atomic positions that require this reindexing is shown in Figure 3. The redefinition of the unit cell results in a change in the formula units per cell from 4 to 2. Despite the change in lattice parameters, the misfit parameters $1+\delta$ (the ratio of the in-plane packing density between the two constituents) only range from 1.20 to 1.24, which are within error of one other. The change in SnSe structure with thickness suggests that the energetic cost of distorting the interior of the SnSe layer to achieve a lattice match is higher than the energy gain resulting from a more coherent interface with $TiSe_2$. In the $m = 1$ case, however, there are no interior atoms to compete with the surface stabilization gained by the tetragonal distortion.

HAADF-STEM was collected to further probe the layering, in-plane structure, and connectivity between the layers of the compounds. Representative images are shown in Figure 4. The two constituents are distinguished by the different contrasts in the image, with the SnSe layers appearing brighter and the $TiSe_2$ appearing darker. The interfaces between the different constituents in all images are atomically abrupt and smooth, reflecting diffusion during the self-assembly process, which corrects for local variations in either thickness or composition. Where zone axes are observed for the darker $TiSe_2$ layers, they

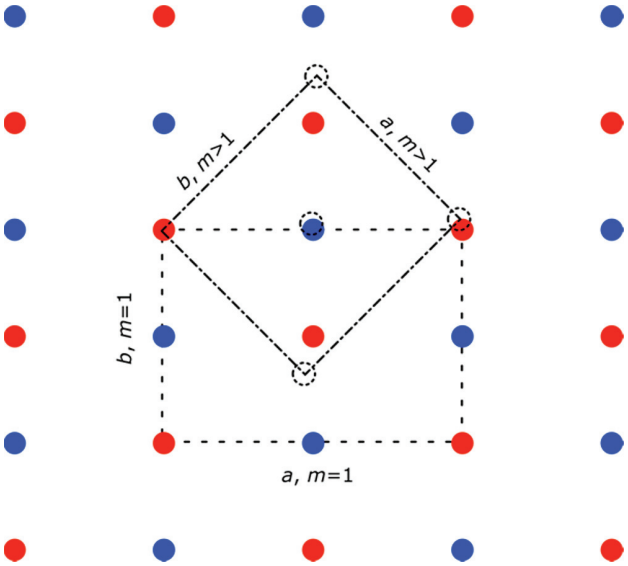

Figure 3. Schematic of shifting atomic positions of the SnSe constituent of $[(SnSe)_{1+\delta}]_mTiSe_2$ causing a redefinition of the in-plane unit cell from the $m = 1$ compound to the $m \geq 2$ compounds.

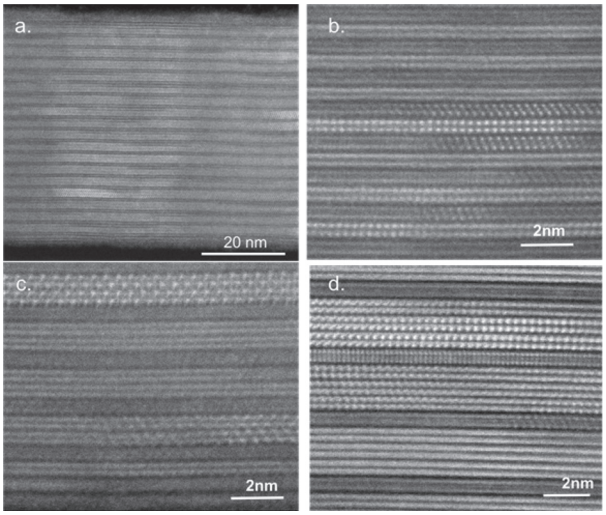

Figure 4. HAADF-STEM images of $[(SnSe)_{1+\delta}]_mTiSe_2$ compounds ($m \leq 3$). (a) Image of $(SnSe)_{1.20}TiSe_2$ showing the consistent alternation of the two constituent structures throughout the entire film. The bright layers correspond to SnSe, while the darker layers correspond to $TiSe_2$. (b) Enlarged image of $[(SnSe)_{1.20}]_1TiSe_2$ showing the local atomic structure. Repeating orientations in some areas of the film support previous reports of regions of long-range coherence. (c) Magnified image of $[(SnSe)_{1.24}]_2TiSe_2$ showing the pairing of the SnSe layers. Multiple orientations for the same constituent are observed throughout the film, demonstrating the turbostratic disorder present in all compounds. (d) Expanded image of $[(SnSe)_{1.20}]_3TiSe_2$ showing the disorder between the different bilayers of SnSe.

are those expected for a CdI_2-structured $TiSe_2$ with octahedrally coordinated Ti. The SnSe layers are consistent with the in-plane diffraction data. Figure 4a shows that the sequence of layers is consistently repeated throughout the entire film, in agreement with the diffraction data.

The images of the $m = 1$, $m = 2$, and $m = 3$ compounds, Figure 4b, c, and d, respectively, show that the targeted

DOI: 10.1021/acsnano.7b07506
ACS Nano 2018, 12, 1285−1295

structures were prepared. Small regions with substitutional defects, where $TiSe_2$ replaces a portion of a SnSe bilayer, can occasionally be found when surveying all of the images.[40] These types of substitutional defects that have been observed previously in ferecrystalline compounds are an artifact of the self-assembly and correlated with small deviations in precursor composition from that of the targeted compound.[41,42] Small regions of $SnSe_2$ are also observed at the surface and the film/substrate interface in some films (Figure S5 in the Supporting Information), explaining the low-intensity $SnSe_2$ reflection observed in the in-plane diffraction. This surface $SnSe_2$ is postulated to form as excess Sn and Se migrate out of the sample as the superstructure self-assembles.

The HAADF-STEM images provide information about the alignment between constituent layers at the atomic level that is absent from the diffraction data due to the preferred alignment and turbostratic disorder. Regions with long-range order and regions of rotational disorder are observed in the $m = 1$ compound (Figure 4b).[28] In the $m \geq 2$ images no long-range order between the constituent layers is observed. The extensive rotational disorder between SnSe and $TiSe_2$ layers is consistent with the independent in-plane lattice parameters determined from the X-ray diffraction patterns. The rotational disorder in the $m \geq 2$ compounds is consistent with previous reports of $[(SnSe)_{1+\delta}]_m[TSe_2]_n$ compounds synthesized using the modulated elemental reactants approach.[24,25]

The STEM images reveal several structural changes and stacking sequences in SnSe layers that are not expected from the bulk structure. The SnSe layers in compounds with $m \geq 2$ distort, forming pairs of atomic planes referred to in the following as bilayers. A similar distortion into pairs of layers was observed for thin PbSe layers and rationalized as an interplay between volume and surface free energy.[14] The spacing between bilayers is larger than the spacing within them, consistent with distorted α-SnSe (GeS structure) or β-SnSe (TlI structure) and in contrast to the equally spaced atomic planes in a rock salt structure (Figure 4c and d). Where zone axes are observed for the SnSe layers, most of the layers stack on top of one another with the cations alternating with the anions in a face-centered arrangement, which is consistent with a distorted rock salt structure, but also with the (100) zone axis of α-SnSe and β-SnSe. Occasionally, the bilayers stack with the cations aligned above each other, as found along the (010) axis of the bulk α-SnSe structure and the (001) axis of the bulk β-SnSe structure, sometimes even within the same layer, as evident in areas highlighted in Figure 5. These unexpected stacking arrangements may reflect either the mechanism of formation[43] or the competition between the different SnSe structures.

DFT calculations were undertaken to understand the changes in structure of the SnSe layer with thickness and the shift in the location of different bilayers with respect to one another. In doing these calculations, there were two approximations to choose between. One option would be to create a supercell and distort the structure of both constituents. Since the observed structures are not distorted and the layer orientation in the $m = 2-4$ compounds is random from layer to layer, this is a significant approximation. The other choice was to calculate the energy of isolated layers of each constituent, focusing on the energy differences between different constituents as a function of the thickness of the layer. Since creating a supercell would force a distortion in the structure of the layer whose structure we are trying to understand, we limited our calculations to vacuum-isolated SnSe layers of different thickness.

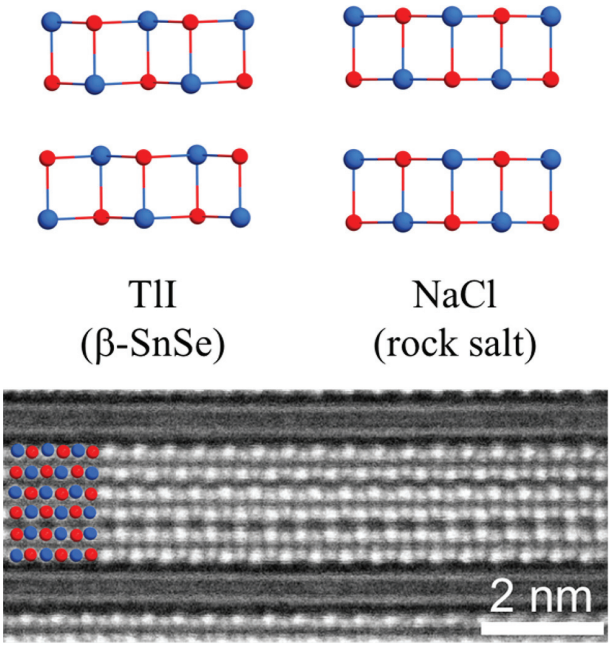

Figure 5. Expanded HAADF-STEM image showing two different SnSe orientations within the same layer of $[(SnSe)_{1+\delta}]_mTiSe_2$.

DFT calculations were carried out on isolated multilayers ($1 \leq m \leq 4$) using four different SnSe structures, as shown in Figure 6, to probe the observed structure changes as m is increased. Figure 7 shows the evolution of the lattice parameters as a function of the number of bilayers. The GeS structure is the only structure type where the lattice parameters change significantly with thickness. The lattice parameters trend toward the calculated lattice parameters of the bulk structure at

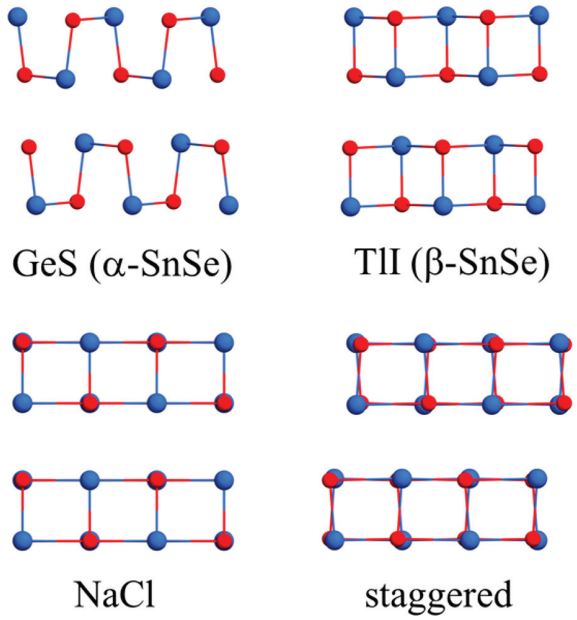

Figure 6. Relaxed structures of two SnSe bilayers for the different polytypes used in the DFT calculations viewed along the [010] axis. Sn atoms are blue and Se atoms are red.

DOI: 10.1021/acsnano.7b07506
ACS Nano 2018, 12, 1285−1295

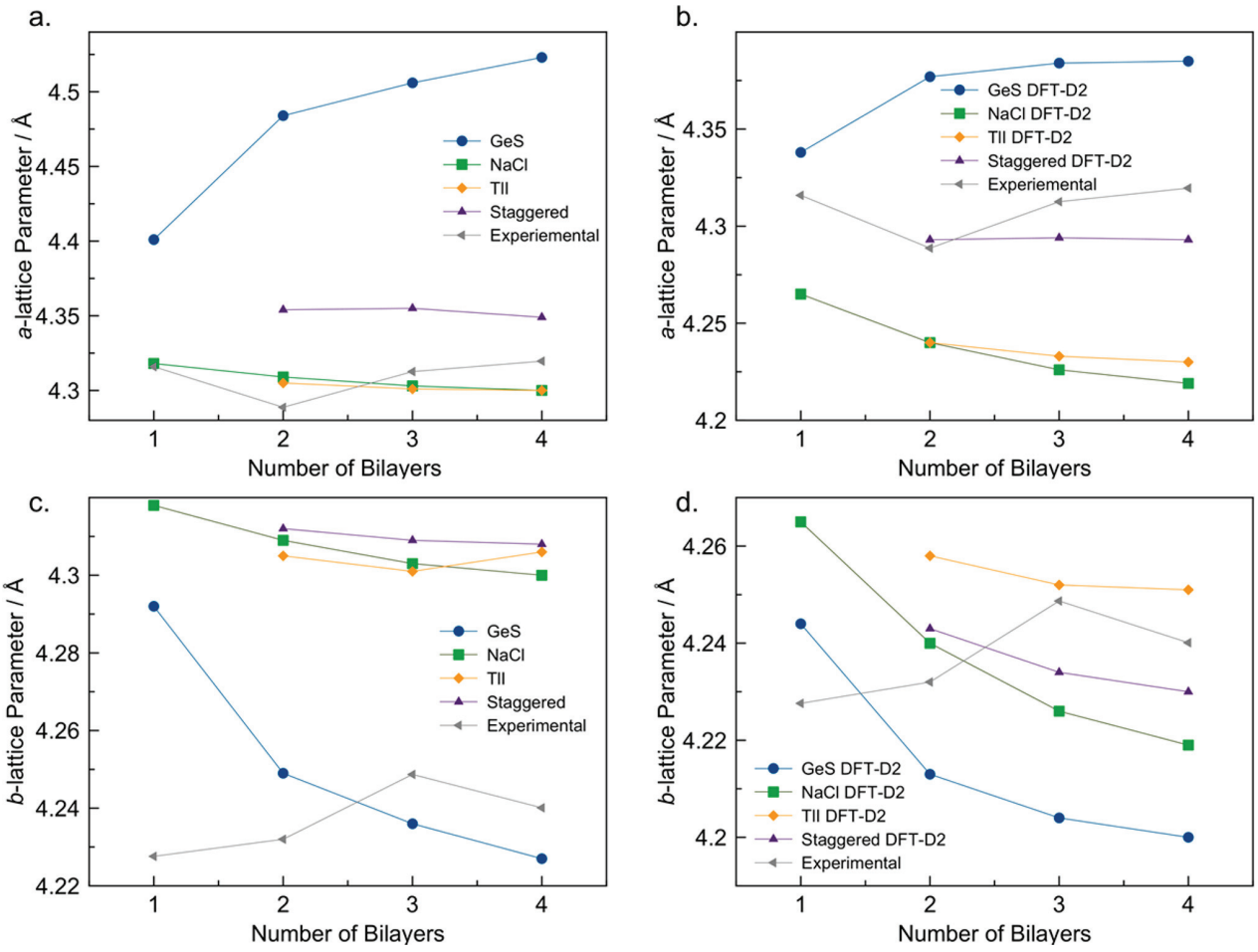

Figure 7. In-plane lattice parameters for the *a*-axis (a, b) and the *b*-axis (c, d) of the different SnSe polymorphs as a function of the number of bilayers. (a) and (c) were calculated without a van der Waals functional. (b) and (d) were calculated with the DFT-D2 van der Waals functional. Including the DFT-D2 van der Waal's functional does not change the trends in lattice parameters of the polymorphs as the number of bilayers is increased. The lattice parameters for the NaCl and staggered structures are given in their primitive lattices. The experimental lattice parameters for $m = 1$ were normalized to give a better comparison to the lattice parameters for $m > 1$.

room temperature (a = 4.56 Å, b = 4.21 Å) as thickness is increased. This is consistent with DFT calculations using the optB88 functional published elsewhere[44] and with the experimental data for SnSe layers as a function of thickness in ferecrystals with a variety of dichalcogenide layers.[27] The lattice parameters for the GeS and NaCl-structured bulk structures are larger than the experimental bulk and thin film lattice parameters (GeS: a = 4.450 Å, b = 4.153 Å;[21] NaCl: a = 5.99 Å[45]), as expected from generalized-gradient approximation (GGA). The calculated bulk TlI structure, on the other hand, has smaller lattice parameters (a = 4.301 Å, b = 11.808 Å, c = 4.293 Å) than those experimentally determined in bulk β-SnSe at 825 K (a = 4.310 Å, b = 11.705 Å, c = 4.318 Å,).[21] The staggered structure converges to a rectangular basal plane, even when started as a square lattice. To account for possible van der Waals interactions, we also included dispersion corrections using Grimme's DFT-D2 method.[46] Including these corrections results in improved bulk lattice parameters for α-SnSe (a = 4.407 Å, b = 4.185 Å, c = 11.626 Å) and NaCl-structured SnSe (a = 5.949 Å). For β-SnSe, the lattice parameters are further decreased (a = 4.218 Å, b = 11.675 Å, c = 4.245 Å). The lattice parameters obtained with DFT-D2 follow the same trend for isolated layers as when using the uncorrected Perdew–Burke–Ernzerhof (PBE), albeit with smaller lattice parameters and a/b ratios. The structures of the isolated layers distort along the c-axis, where the Se atoms are distorted into the vacuum region with respect to the Sn atoms, except for the single bilayer, where the Sn atoms are distorted into the vacuum region. The degree of distortion increases with increasing number of bilayers from 0.01 to 0.04 Å (0.02 to 0.09 Å for DFT-D2). Layers adjacent to the vacuum region show larger distortions than layers adjacent to other SnSe layers. The trends of the distortion with m are consistent with structural refinements of SnSe layers observed in $[(SnSe)_{1+\delta}]_m[(NbSe_2)]_n$ and $[(SnSe_{1+\delta})]_m[(MoSe_2)]_n$,[25,47] although the magnitude is smaller than observed experimentally.

Total energies were calculated for each of the structures for different thicknesses, as shown in Table 2. The GeS structure has the lowest total energy per formula unit (f.u.) for all investigated numbers of bilayers. The TlI structure is 15–17 meV/f.u. higher in energy than GeS, and this energy difference is nearly independent of the thickness of SnSe. The energy differences to the NaCl structure and its staggered derivative systematically increase relative to the GeS structure as the SnSe thickness is increased. While the trends are similar when dispersion corrections are included, the magnitude of the

DOI: 10.1021/acsnano.7b07506
ACS Nano 2018, 12, 1285–1295

Table 2. Total Energy Differences per Formula Unit ΔE_{GeS} of the Polymorphs with Respect to the GeS (α-SnSe) Structure as a Function of the Number of Bilayers[a]

	energy of various structure types (meV) referenced to that of GeS		
layer	TlI	NaCl	staggered
1		3 (2)	
2	15 (3)	11 (51)	12 (35)
3	16 (4)	15 (60)	17 (45)
4	15 (4)	17 (62)	19 (51)

[a]Values in parentheses represent values obtained using DFT-D2.

energy differences changes significantly for $m \geq 2$. Using DFT-D2, the TlI structure is much closer in energy to the GeS structure (<5 meV/f.u.), and the NaCl structure is much higher in energy (>50 meV/f.u.). This suggests that there are significant van der Waals interactions in the GeS and TlI structures that stabilize them compared to the rock-salt-type structures. For one bilayer, however, the energy difference between the GeS and the NaCl structure is only 3 meV/f.u. (2 meV/f.u. using DFT-D2), indicating that both structures are almost equally stable. This also suggests that van der Waals interactions primarily occur between and not within the bilayers. It is known that in ferecrystals, compounds with SnSe monolayers can, depending on the adjacent transition metal dichalcogenide, adopt square (V, Mo, Ta) or rectangular (Ti, Nb) basal planes.[27] To probe the energy penalty for creating the rectangularly distorted NaCl lattice, additional calculations were performed. Calculations with a rectangular NaCl starting structure lattice converged to a square structure. However, relaxing only the atomic positions and the in-plane lattice parameters while keeping the a/b ratio fixed at the experimentally determined ratio yields a rectangular structure with a total energy that is only 3 meV/f.u. larger than the undistorted NaCl structure. The relaxed lattice parameters, 6.169 and 6.047 Å (6.094 and 5.974 Å using DFT-D2) for the a-axis and the b-axis, respectively, are in good agreement with the experimental lattice parameters for $(SnSe)_{1.20}TiSe_2$. Any surface stabilization by forming a commensurate interface with the $TiSe_2$ layers is not included in these calculations, so the small energy difference in our calculations suggests that a single SnSe bilayer can easily distort to form a commensurate lattice with $TiSe_2$. However, additional interactions must be present that raise the energy of the GeS structure above the energy of the NaCl structure.

For $m > 1$, the energy of the NaCl structure per formula unit increases significantly relative to GeS and TlI due to the stabilizing effect of van der Waals interactions in the GeS and TlI structures. Hence, it is not energetically favorable to maintain a lattice match with the $TiSe_2$ layers. Instead, the symmetry of the in-plane lattice is consistent with the GeS or TlI structure with a steadily increasing a-axis lattice parameter and a nearly constant b-axis lattice parameter. This behavior is consistent with the DFT results of GeS-structured SnSe layers, albeit with a much smaller slope. The values of the experimental lattice parameters on the other hand are more consistent with the TlI structure. The transition from the GeS to the TlI structure is second order, and the observed (100) reflection in the in-plane diffraction pattern should be extinct in either structure, suggesting that neither structure describes the in-plane symmetry completely. The interactions with the $TiSe_2$ layers that raise the energy of the GeS structure above the energy of the NaCl structure for $m = 1$ could also raise the energy of the GeS structure to a value similar to the energy of the TlI structure for $m > 1$, resulting in a competition between these two structure types. It is thus plausible that the actual structure is an interpolation between the GeS and the TlI structure, which cannot be determined conclusively without including the interactions between the $TiSe_2$ and SnSe layers. More experimental evidence is needed to determine the exact structure (or structures) the SnSe layers adopt for $m = 2$ and 3. These results, in combination with experimental data, suggest that the van der Waals interactions inside the SnSe layers significantly stabilize the GeS and the TlI structures, resulting in a competition between these two structures during growth.

The HAADF-STEM image of $[(SnSe)_{1.20}]_3TiSe_2$ (Figure 4d) shows SnSe layers that are inconsistent with any zone axis of a single SnSe structure, but instead show a single β-SnSe unit cell with half of another β-SnSe unit cell shifted by half a lattice constant. DFT calculations on these shifted unit cells show only a small energy difference between them and undistorted β-SnSe with three bilayers (see Supporting Information Figure S6 and Table S1). Since Sn(II) has a lone pair, we calculated the electron localization functions (ELFs) for the different structures and layer thicknesses. For the GeS structure, the Sn atoms in the surface layer have prominent ELFs that project out into the vacuum. The Sn atoms in the inner layer have less pronounced lone pairs again pointed outward toward the adjacent bilayer. Thus, the interface consists of lone pair electrons of Sn and Se in each bilayer projected toward each other. This suggests that there is little penalty to grow these layers with or without this defect, so the structure of SnSe with three bilayers may depend entirely on nucleation and growth kinetics.

The structural changes with thickness also result in changes in the electronic structure, which will impact the trends in transport properties of these compounds. Temperature-dependent resistivity data collected on the title compounds are shown in Figure 8. The resistivities of the $m = 2$, 3, and 4 compounds are all larger than the previously reported $m = 1$ compound.[31] The highest resistivity measured is for the $m = 2$ compound, with subsequent increases in m resulting in lower

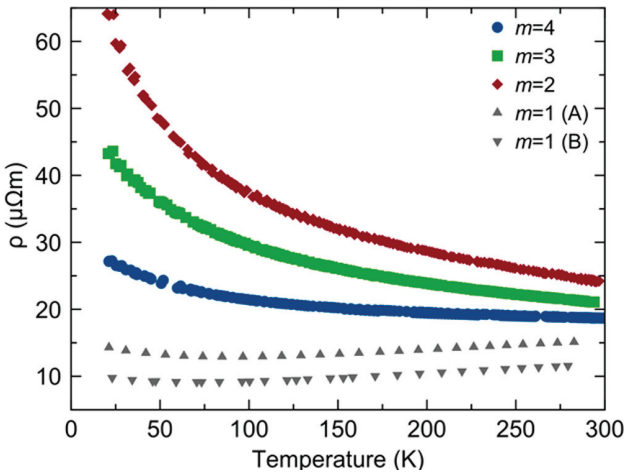

Figure 8. Temperature-dependent resistivity measurements of the $[(SnSe)_{1+\delta}]_mTiSe_2$ compounds with $m = 1$–4. Measurements of two different $m = 1$ samples are plotted to show reproducibility of their behavior.

DOI: 10.1021/acsnano.7b07506
ACS Nano 2018, 12, 1285–1295

resistivity. This behavior is opposite that observed previously for $[(SnSe)_{1+\delta}]_mNbSe_2$, where an increase in the thickness of SnSe resulted in a systematic increase in resistivity.[44] This difference reflects the impact of structural changes with thickness of the SnSe layer and interactions between the layers on the electronic properties of these materials. At low temperatures, the resistivity increases as temperature is decreased for all compounds, where the overall magnitude of this upturn decreases with increasing m. The increase in resistivity is not exponential as expected for a traditional semiconductor and is not pronounced enough to suggest a metal−insulator transition.[48] The much weaker temperature dependence is consistent with a metal or heavily doped semiconductor where carrier localization is occurring at low temperatures, but the possibility of the upturn being the result of a charge density wave in the $TiSe_2$ layer cannot be excluded.[49,50] Similar upturns in resistivity are observed at low temperatures in $[(PbSe)_{1+\delta}]_m[TiSe_2]_n$ compounds. In the $[(PbSe)_{1+\delta}]_m[TiSe_2]_n$ compounds, however, there is a decrease in resistivity as temperature is decreased prior to the upturn.

Hall effect measurements (Figure 9) were collected to provide additional information about the electronic properties.

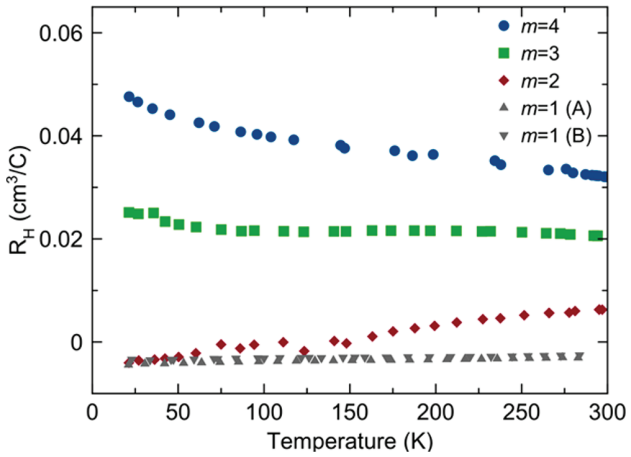

Figure 9. Temperature-dependent Hall coefficients for $[(SnSe)_{1+\delta}]_mTiSe_2$ compounds.

For all compounds, the Hall coefficient changes only slightly with temperature in an approximately linear fashion, which is inconsistent with semiconducting behavior. This suggests the low-temperature upturns in resistivity are caused by a change in mobility with temperature or a more complex two-carrier behavior. The Hall coefficient varies systematically with m and changes sign as m is increased. The Hall coefficient for the m = 1 compound is negative and stays constant with temperature, as expected for a simple metal, indicating electrons are the majority carrier. The Hall coefficient for the m = 2 compound decreases as the temperature is lowered, switching sign at approximately 160 K, indicating a change in the majority carrier type from holes to electrons. The m = 3 compound has a positive Hall coefficient at all temperatures, and the m = 4 compound has a larger positive Hall coefficient at all temperatures. The positive room-temperature Hall coefficients suggest holes are the majority carrier. The changes in the magnitude of the Hall coefficient as m increases and the positive signs are not consistent with prior models, where transport properties were assumed to be dominated by electrons in $TiSe_2$ resulting from charge donation from SnSe to $TiSe_2$. The magnitude of the Hall coefficients as m increases and as temperature is decreased, combined with the resistivity data discussed previously, also suggests that the average carrier mobility significantly increases as m is increased and varies with temperature.

Room-temperature Seebeck coefficients (α) were measured for all the compounds to gain more information about the change of carrier type as m and temperature are varied. The results are summarized in Table 3. Like the Hall coefficient, the Seebeck coefficient also changes sign as m is increased. The sign of the Seebeck coefficient agrees with the sign of the Hall coefficient for m = 1, 3, and 4, indicating agreement in majority carrier type. The m = 2 compound, however, displays a positive Hall coefficient and a negative Seebeck coefficient, which indicates that both carrier types contribute to the observed conductivity. This is consistent with the change in the Hall coefficient as a function of temperature.

Table 3. Room-Temperature Transport Properties for $[(SnSe)_{1+\delta}]_mTiSe_2$ Compounds

m	$\rho(T = 295\ K)$ ($\mu\Omega$m)	R_H (cm^3/C)	α (μV/K)
1 (A)	15(1)	−0.0044(1)	−75(3)
1 (B)	12(1)	−0.0034(1)	−77(3)
2	24(1)	0.0064(1)	−29(1)
3	21(1)	0.021(1)	2(1)
4	19(1)	0.032(1)	22(1)

Historically, the band structures of both misfit layer compounds and ferecrystals have been discussed using a rigid band approximation, with MX bands and TX_2 bands only slightly perturbed by the interface and the charge transfer between them.[51] For most misfit layer compounds and ferecrystals containing $TiSe_2$ it appears that the rock salt layers "dope" the dichalcogenides, which then dominate transport. For example in the analogous $[(PbSe)_{1+\delta}]_m[TiSe_2]_n$ compounds where $m = n$,[52] a donor−acceptor behavior between the PbSe and $TiSe_2$ layers was suggested and the establishment of a space-charge region near the interface was used to describe the transport. The data are consistent with the relative position of the Fermi level remaining unchanged as m and n are simultaneously increased. The trends in the transport properties as m is varied in $[(SnSe)_{1+\delta}]_mTiSe_2$ are more complicated as the band structure is being altered due to structural distortions within the SnSe constituent and the ratio of m to n is also being changed.

The complex variation of the structure and electrical properties indicates that these compounds cannot be thought of as simple composites where the properties of the individual constituents can be summed to obtain the properties of the intergrowth. DFT, XRD, and STEM data all indicate that the structure of the SnSe constituent is changing with thickness and that the interactions between the SnSe and $TiSe_2$ are important. Charge transfer is likely a function of structure, the m/n ratio, and the interaction between the constituents. The changes in transport properties reflect the change in SnSe structure with thickness. Given the second-order phase transition in bulk SnSe with temperature, it is likely that the changes in the temperature dependence of the electrical data could result from structural transitions with temperature.

DOI: 10.1021/acsnano.7b07506
ACS Nano 2018, 12, 1285−1295

CONCLUSIONS

Three new $[(SnSe)_{1+\delta}]_mTiSe_2$ compounds were synthesized using modulated elemental reactants as precursors. Control of the nanoarchitecture was achieved by systematically increasing the number of SnSe layers in the repeating unit of the precursor. As the SnSe block thickness is increased, the basal plane structure of SnSe evolves from rectangular (m = 1) to an orthorhombic GeS related structure (m = 4) with the m = 2 and 3 compounds having related distorted structures. This evolution indicates that the energetic cost of distorting to form an epitaxial interface with $TiSe_2$ increases as the number of interior layers increases. This is consistent with DFT calculations and can be attributed to stabilizing van der Waals interactions. For SnSe blocks with m = 3, shear defects are observed within the same repeating unit. DFT calculations showed that the different shear structures and the undistorted structure of β-SnSe are very close in energy, suggesting that the existence of these defects depends on nucleation and growth kinetics. The compounds also display unexpectedly complex electrical properties, with resistivity decreasing as the thickness of the SnSe layer is increased and the carrier type changing as m and temperature are varied. The evolving structure and electrical properties suggest the interactions between constituents are complicated and the previously used simple models based on rigid bands and charge transfer between the constituents is not appropriate for these compounds. Further investigations into this behavior are necessary to fully understand the cause of the upturn at low temperatures in the resistivity and the change in carrier type with increasing number of SnSe layers.

EXPERIMENTAL SECTION

Precursors were synthesized in a high-vacuum physical vapor deposition system, with depositions occurring at pressures below 5×10^{-7} Torr. Tin (Alfa Aesar, 99.98%) and titanium (Alfa Aesar, 99.99%) metals were deposited using electron beam guns, and selenium was deposited using an effusion cell. A computer-controlled pneumatic shutter system was used to control the sequence and thickness of the elemental layers.[53] The rate of deposition and the thickness of the elemental layers were measured using quartz crystal microbalances, with rates maintained at 0.1−0.3 Å/s at the substrate. The elemental layers were deposited in a $\{Ti-Se-(Sn-Se)_m\}$ sequence, with the number of sequential Sn|Se repeats, m, equal to the number of Sn−Se bilayers desired in the targeted compounds. The $\{Ti-Se-(Sn-Se)_m\}$ sequence was repeated to get a total film thickness of approximately 500 Å, a thickness convenient for thin-film diffraction and electrical property measurements. Samples were prepared on either (100) Si with a SiO_2 native oxide layer for structural and compositional characterization or fused silica for electrical characterization. Composition measurements used for the calibration of deposition parameters was performed using EPMA using a method described by Donovan *et al.*[54] The precursors were annealed in an inert nitrogen environment ($p[O_2] \leq 0.8$ ppm) at 350 °C for 30 min to self-assemble the mostly amorphous precursors into the desired products.

The structures of the precursors and products were determined using XRD and electron microscopy studies. Specular XRD and XRR were used to determine the compound's superstructure and the total film thickness, respectively, using a Bruker D8 Discover. Constituent in-plane structures were characterized using an in-plane diffraction geometry on a Rigaku SmartLab diffractometer. All diffraction experiments were conducted using a Cu Kα radiation source with a nickel filter used to remove any Cu Kβ radiation. In-plane lattice parameters were refined with the Le Bail method[36] using the FullProf suite, which takes into account signals from both the Cu Kα(1) and Cu Kα(2) radiation.[55,56]

HAADF-STEM data were collected at Pacific Northwest National Laboratory using a probe aberration-corrected FEI Titan 80-300 STEM. Electron-transparent cross-sectional lamellae of the samples were prepared using an FEI Helios 600 Ga^+ focused ion beam. A procedure was employed similar to the Wedge Prep method described by Schaffer[57] with final thinning and polishing performed using 2 keV ions.

Electrical resistivity and Hall effect measurements were conducted utilizing the van der Pauw geometry on a homemade closed-cycle helium low-temperature system using samples deposited on fused silica. Magnetic fields ranging from 0 to 16 kG were applied to the sample during the van der Paaw Hall measurement. The magnetic field was increased in steps, so five data points were taken for each of the four lead configurations. A straight line was fit to the change in Hall voltage as a function of field to obtain the Hall coefficient. Seebeck measurements were made on bar-shaped samples with copper-constantan thermocouples. In this experiment, one end of the sample was cooled and the voltage between the same material thermocouple leads was measured.

DFT calculations were performed using the Vienna *ab initio* simulation (VASP) package.[58−60] The projector augmented wave (PAW)[61,62] method was used to describe the interactions between the core and the valence electrons. Exchange and correlation were described using PBE functionals in the GGA.[63] A cutoff energy of 500 eV was used for all calculations. Calculations were carried out on isolated multilayers using a 15 × 15 × 1 Monkhorst−Pack[64] grid for GeS- and TlI-structured layers and a 11 × 11 × 1 Monkhorst−Pack grid for the other layers. To minimize interactions between periodic images, vacuum spacing of at least 20 Å was included between each multilayer. For bulk calculations, Monkhorst−Pack grids of 15 × 15 × 5, 15 × 5 × 15, and 11 × 11 × 11 were used for the GeS structure, the TlI structure, and the NaCl structure, respectively. Self-consistency was achieved with an energy convergence of 10^{-6} eV. Atomic positions and in-plane lattice parameters were allowed to relax until the forces were smaller than 0.005 Å/eV and the stresses were smaller than 0.01 GPa. For α-SnSe, rock salt (NaCl structure, $Fm\bar{3}m$), and a staggered rock-salt-related structure, (001) slabs of the bulk structures were used, and a (010) slab was used for β-SnSe. The calculations were carried out on two, three, and four bilayers of each polytype and additionally on a single bilayer for the GeS and NaCl structures. Dispersion corrections were included using Grimme's DFT-D2 functional.[46] We chose this functional because it gave the best agreement with the bulk SnSe structure.

ASSOCIATED CONTENT

Supporting Information

The Supporting Information is available free of charge on the ACS Publications website at DOI: 10.1021/acsnano.7b07506.

Le Bail fits of $[(SnSe)_{1+\delta}]_mTiSe_2$ compounds with $m \leq 4$, HAADF-STEM image of $(SnSe)_{1.2}TiSe_2$ with $SnSe_2$ on the surface, and DFT calculations on distortions of three SnSe bilayers with TlI structure (PDF)

AUTHOR INFORMATION

Corresponding Author

*E-mail: davej@uoregon.edu.

ORCID

Danielle M. Hamann: 0000-0002-9262-1060

David C. Johnson: 0000-0002-1118-0997

Author Contributions

The manuscript was written through contributions of all authors.

Notes

The authors declare no competing financial interest.

DOI: 10.1021/acsnano.7b07506
ACS Nano 2018, 12, 1285−1295

ACKNOWLEDGMENTS

This material is based upon work supported by the National Science Foundation Graduate Research Fellowship Program under Grant No. 1309047 for D.M.H. Any opinions, findings, and conclusions or recommendations expressed in this material are those of the author(s) and do not necessarily reflect the views of the National Science Foundation. A.C.L. acknowledges support from the University of Oregon Office of the Vice President of Research and Innovation. The authors acknowledge support from the National Science Foundation under Grant DMR-1710214. We would like to acknowledge the Center for Advanced Materials Characterization in Oregon (CAMCOR) at the University of Oregon. For computational resources, the authors acknowledge the University of Oregon ACISS cluster (National Science Foundation OCI-0960354). We acknowledge support through the Collaborative Access Team (CAT): Pooled Resources for Electron Microscopy Informatics, Education and Research (PREMIER) Network Program at Pacific Northwest National Laboratory (PNNL) and the Environmental Molecular Sciences Laboratory, a national scientific user facility sponsored by DOE's Office of Biological and Environmental Research at PNNL. PNNL is a multiprogram national laboratory operated by Battelle for DOE under Contract DE-AC05-76RL01830.

REFERENCES

(1) Novoselov, K. S.; Geim, A. K.; Morozov, S. V.; Jiang, D.; Zhang, Y.; Dubonos, S. V.; Grigorieva, I. V.; Firsov, A. A.; Novoselov, K. S. Electric Field Effect in Atomically Thin Carbon Films. *Science* **2007**, *306*, 183−191.

(2) Novoselov, K. S. Nobel Lecture: Graphene: Materials in the Flatland. *Rev. Mod. Phys.* **2011**, *83*, 837−849.

(3) Geim, A. K. Nobel Lecture: Random Walk to Graphene. *Rev. Mod. Phys.* **2011**, *83*, 851−862.

(4) Hamann, D. M.; Hadland, E. C.; Johnson, D. C. Heterostructures Containing Dichalcogenides-New Materials with Predictable Nanoarchitectures and Novel Emergent Properties. *Semicond. Sci. Technol.* **2017**, *32*, 93004.

(5) Jariwala, D.; Marks, T. J.; Hersam, M. C. Mixed-Dimensional van Der Waals Heterostructures. *Nat. Mater.* **2017**, *16*, 170−181.

(6) Mak, K. F.; Lee, C.; Hone, J.; Shan, J.; Heinz, T. F. Atomically Thin MoS_2: A New Direct-Gap Semiconductor. *Phys. Rev. Lett.* **2010**, *105* (13)10.1103/PhysRevLett.105.136805.

(7) Zhao, W.; Ghorannevis, Z.; Chu, L.; Toh, M.; Kloc, C.; Tan, P.-H.; Eda, G. Evolution of Electronic Structure in Atomically Thin Sheets of WS_2 and WSe_2. *ACS Nano* **2013**, *7*, 791−797.

(8) Komsa, H.-P.; Krasheninnikov, A. V. Electronic Structures and Optical Properties of Realistic Transition Metal Dichalcogenide Heterostructures from First Principles. *Phys. Rev. B: Condens. Matter Mater. Phys.* **2013**, *88*, 85318.

(9) Ulstrup, S.; Čabo, A. G.; Miwa, J. A.; Riley, J. M.; Grønborg, S. S.; Johannsen, J. C.; Cacho, C.; Alexander, O.; Chapman, R. T.; Springate, E.; Bianchi, M.; Dendzik, M.; Lauritsen, J. V.; King, P. D. C.; Hofmann, P. Ultrafast Band Structure Control of a Two-Dimensional Heterostructure. *ACS Nano* **2016**, *10*, 6315−6322.

(10) Ugeda, M. M.; Bradley, A. J.; Shi, S.-F.; da Jornada, F. H.; Zhang, Y.; Qiu, D. Y.; Ruan, W.; Mo, S.-K.; Hussain, Z.; Shen, Z.-X.; Wang, F.; Louie, S. G.; Crommie, M. F. Giant Bandgap Renormalization and Excitonic Effects in a Monolayer Transition Metal Dichalcogenide Semiconductor. *Nat. Mater.* **2014**, *13*, 1091−1095.

(11) Grubišić Čabo, A.; Miwa, J. A.; Grønborg, S. S.; Riley, J. M.; Johannsen, J. C.; Cacho, C.; Alexander, O.; Chapman, R. T.; Springate, E.; Grioni, M.; Lauritsen, J. V.; King, P. D. C.; Hofmann, P.; Ulstrup, S. Observation of Ultrafast Free Carrier Dynamics in Single Layer MoS_2. *Nano Lett.* **2015**, *15*, 5883−5887.

(12) Bruix, A.; Miwa, J. A.; Hauptmann, N.; Wegner, D.; Ulstrup, S.; Grønborg, S. S.; Sanders, C. E.; Dendzik, M.; Grubišić Čabo, A.; Bianchi, M.; Lauritsen, J. V.; Khajetoorians, A. A.; Hammer, B.; Hofmann, P. Single-Layer MoS_2 on Au(111): Band Gap Renormalization and Substrate Interaction. *Phys. Rev. B: Condens. Matter Mater. Phys.* **2016**, *93*, 165422.

(13) Geim, A. K.; Grigorieva, I. V. Van Der Waals Heterostructures. *Nature* **2013**, *499*, 419−425.

(14) Anderson, M. D.; Heideman, C. L.; Lin, Q.; Smeller, M.; Kokenyesi, R.; Herzing, A. A.; Anderson, I. M.; Keszler, D. A.; Zschack, P.; Johnson, D. C. Size-Dependent Structural Distortions in One-Dimensional Nanostructures. *Angew. Chem., Int. Ed.* **2013**, *52*, 1982−1985.

(15) Smeller, M. M.; Heideman, C. L.; Lin, Q.; Beekman, M.; Anderson, M. D.; Zschack, P.; Anderson, I. M.; Johnson, D. C. Structure of Turbostratically Disordered Misfit Layer Compounds $[(PbSe)_{0.99}]_1[WSe_2]_1$, $[(PbSe)_{1.00}]_1$ $[MoSe_2]_1$, and $[(SnSe)_{1.03}]_1$. *Z. Anorg. Allg. Chem.* **2012**, *638*, 2632−2639.

(16) Feng, W.; Zhou, H.; Chen, F. Impact of Thickness on Crystal Structure and Optical Properties for Thermally Evaporated PbSe Thin Films. *Vacuum* **2015**, *114*, 82−85.

(17) Alemayehu, M. B.; Falmbigl, M.; Ta, K.; Grosse, C.; Westover, R. D.; Bauers, S. R.; Fischer, S. F.; Johnson, D. C. Structural and Electrical Properties of $([SnSe]_{1+\delta})_m(NbSe_2)_1$ Compounds: Single $NbSe_2$ Layers Separated by Increasing Thickness of SnSe. *Chem. Mater.* **2015**, *27*, 867−875.

(18) Bauers, S. R.; Merrill, D. R.; Moore, D. B.; Johnson, D. C. Carrier Dilution in $TiSe_2$ Based Intergrowth Compounds for Enhanced Thermoelectric Performance. *J. Mater. Chem. C* **2015**, *3*, 10451−10458.

(19) Falmbigl, M.; Fiedler, A.; Atkins, R. E.; Fischer, S. F.; Johnson, D. C. Suppressing a Charge Density Wave by Changing Dimensionality in the Ferecrystalline Compounds $([SnSe]_{1.15})_1(VSe_2)_n$ with n = 1, 2, 3, 4. *Nano Lett.* **2015**, *15*, 943−948.

(20) Helmholz, L. The Crystal Structure of the Low-Temperature Modification of Thallous Iodide. *Z. Kristallogr. - Cryst. Mater.* **1936**, *95*, 129−137.

(21) Chattopadhyay, T.; Pannetier, J.; Von Schnering, H. G. Neutron Diffraction Study of the Structural Phase Transition in SnS and SnSe. *J. Phys. Chem. Solids* **1986**, *47* (9), 879−885.

(22) Wiedemeier, H.; von Schnering, H. G. Refinement of the Structures of GeS, GeSe, SnS and SnSe. *Zeitschrift für Krist.* **1978**, *148*, 295−303.

(23) Schnering, H. G. v.; Wiedemeier, H. The High Temperature Structure of β-SnS and β-SnSe and the B16-to-B33 Type λ-Transition Path. *Z. Kristallogr. - Cryst. Mater.* **1981**, *156*, 143−150.

(24) Atkins, R.; Wilson, J.; Zschack, P.; Grosse, C.; Neumann, W.; Johnson, D. C. Synthesis of $[(SnSe)_{1.15}]_m(TaSe_2)_n$ Ferecrystals: Structurally Tunable Metallic Compounds. *Chem. Mater.* **2012**, *24*, 4594−4599.

(25) Beekman, M.; Disch, S.; Rouvimov, S.; Kasinathan, D.; Koepernik, K.; Rosner, H.; Zschack, P.; Neumann, W. S.; Johnson, D. C. Controlling Size-Induced Phase Transformations Using Chemically Designed Nanolaminates. *Angew. Chem., Int. Ed.* **2013**, *52*, 13211−13214.

(26) Alemayehu, M. B.; Falmbigl, M.; Ta, K.; Johnson, D. C. Effect of Local Structure of NbSe2 on the Transport Properties of $[(SnSe)_{1.16}]_1[(NbSe_2)]_n$ Ferecrystals. *Chem. Mater.* **2015**, *27*, 2158−2164.

(27) Falmbigl, M.; Alemayehu, M. B.; Merrill, D. R.; Beekman, M.; Johnson, D. C. In-Plane Structure of Ferecrystalline Compounds. *Cryst. Res. Technol.* **2015**, *50*, 464−472.

(28) Hamann, D. M.; Merrill, D. R.; Bauers, S. R.; Mitchson, G.; Ditto, J.; Rudin, S. P.; Johnson, D. C. Long-Range Order in $[(SnSe)_{1.2}]_1[TiSe_2]_1$ Prepared from Designed Precursors. *Inorg. Chem.* **2017**, *56*, 3499−3505.

(29) Johnson, D. C. Controlled Synthesis of New Compounds Using Modulated Elemental Reactants. *Curr. Opin. Solid State Mater. Sci.* **1998**, *3*, 159−167.

DOI: 10.1021/acsnano.7b07506
ACS Nano 2018, 12, 1285−1295

(30) Esters, M.; Johnson, D. C. Targeted Synthesis of Metastable Compounds and Intergrowths: The Modulated Elemental Reactants Method. In *Crystal Growth: Concepts, Mechanisms, and Applications*; Li, J., Li, J., Chi, Y., Eds.; Nova Science Publishers: New York, 2017; pp 35−118.
(31) Merrill, D. R.; Moore, D. B.; Ditto, J.; Sutherland, D. R.; Falmbigl, M.; Winkler, M.; Pernau, H.-F.; Johnson, D. C. The Synthesis, Structure, and Electrical Characterization of $(SnSe)_{1.2}TiSe_2$. *Eur. J. Inorg. Chem.* **2015**, *2015*, 83−91.
(32) Beekman, M.; Cogburn, G.; Heideman, C.; Rouvimov, S.; Zschack, P.; Neumann, W.; Johnson, D. C. New Layered Intergrowths in the Sn-Mo-Se System. *J. Electron. Mater.* **2012**, *41*, 1476−1480.
(33) Moore, D. B.; Sitts, L.; Stolt, M. J.; Beekman, M.; Johnson, D. C. Characterization of Nonstoichiometric $Ti_{1+x}Se_2$ Prepared by the Method of Modulated Elemental Reactants. *J. Electron. Mater.* **2013**, *42*, 1647−1651.
(34) Moore, D. B.; Stolt, M. J.; Atkins, R.; Sitts, L.; Jones, Z.; Disch, S.; Matt, B.; Johnson, D. C. Structural and Electrical Properties of $(PbSe)_{1.16}TiSe_2$. *Emerging Mater. Res.* **2012**, *1*, 292−298.
(35) Moore, D. B.; Beekman, M.; Disch, S.; Zschack, P.; Häusler, I.; Neumann, W.; Johnson, D. C. Synthesis, Structure, and Properties of Turbostratically Disordered $(PbSe)_{1.18}(TiSe_2)_2$. *Chem. Mater.* **2013**, *25*, 2404−2409.
(36) Le Bail, A.; Duroy, H.; Fourquet, J. L. *Ab-Initio* Structure Determination of $LiSbWO_6$ by X-Ray Powder Diffraction. *Mater. Res. Bull.* **1988**, *23*, 447−452.
(37) Merrill, D. R.; Moore, D. B.; Coffey, M. N.; Jansons, A. W.; Falmbigl, M.; Johnson, D. C. Synthesis and Characterization of Turbostratically Disordered $(BiSe)_{1.15}TiSe_2$. *Semicond. Sci. Technol.* **2014**, *29*, 64004.
(38) Wood, S. R.; Merrill, D. R.; Falmbigl, M.; Moore, D. B.; Ditto, J.; Esters, M.; Johnson, D. C. Tuning Electrical Properties through Control of TiSe2 Thickness in $(BiSe)_{1+\delta}(TiSe_2)_n$ Compounds. *Chem. Mater.* **2015**, *27*, 6067−6076.
(39) Merrill, D. R.; Sutherland, D. R.; Ditto, J.; Bauers, S. R.; Falmbigl, M.; Medlin, D. L.; Johnson, D. C. Kinetically Controlled Site-Specific Substitutions in Higher-Order Heterostructures. *Chem. Mater.* **2015**, *27*, 4066−4072.
(40) Bauers, S. R.; Moore, D. B.; Ditto, J.; Johnson, D. C. Phase Width of Kinetically Stable $([PbSe]_{1+\delta})_1(TiSe_2)_1$ Ferecrystals and the Effect of Precuror Compostion on Electrical Properties. *J. Alloys Compd.* **2015**, *645*, 118−124.
(41) Grosse, C.; Atkins, R.; Kirmse, H.; Mogilatenko, A.; Neumann, W.; Johnson, D. C. Local Structure and Defect Chemistry of $[(SnSe)_{1.15}]_m(TaSe_2)$ Ferecrystals − A New Type of Layered Intergrowth Compound. *J. Alloys Compd.* **2013**, *579*, 507−515.
(42) Falmbigl, M.; Putzky, D.; Ditto, J.; Esters, M.; Bauers, S. R.; Ronning, F.; Johnson, D. C. Influence of Defects on the Charge Density Wave of $([SnSe]_{1+\delta})_1(VSe_2)_1$ Ferecrystals. *ACS Nano* **2015**, *9*, 8440−8448.
(43) Atkins, R.; Moore, D. B.; Johnson, D. C. Insights into the Self-Assembly of Ferecrystalline Compounds from Designed Amorphous Precursors. *Chem. Mater.* **2013**, *25*, 1744−1750.
(44) Fang, W.; Zhang, L.-C.; Qin, G.; Yan, Q.-B.; Zheng, Q.-R.; Su, G. Layer Dependence of Geometric, Electronic and Piezoelectric Properties of SnSe, Electronic and Piezoelectric Properties of SnSe . **2016**, *18*.
(45) Mariano, A. N.; Chopra, K. L. Polymorphism in Some IV-VI Compounds Induced by High Pressure and Thin-Film Epitaxial Growth. *Appl. Phys. Lett.* **1967**, *10*, 282−284.
(46) Grimme, S. Semiempirical GGA-Type Density Functional Constructed with a Long-Range Dispersion Correction. *J. Comput. Chem.* **2006**, *27*, 1787−1799.
(47) Alemayehu, M. B.; Ta, K.; Falmbigl, M.; Johnson, D. C. Structure, Stability, and Properties of the Intergrowth Compounds $([SnSe]_{1+\delta})_m(NbSe_2)_n$, Where $m = n = 1$−20. *J. Am. Chem. Soc.* **2015**, *137*, 4831−4839.
(48) Imada, M.; Fujimori, A.; Tokura, Y. Metal-Insulator Transitions. *Rev. Mod. Phys.* **1998**, *70*, 1039−1263.
(49) Di Salvo, F. J.; Moncton, D. E.; Waszczak, J. V. Electronic Properties and Superlattice Formation in the Semimetal $TiSe_2$. *Phys. Rev. B* **1976**, *14*, 4321−4328.
(50) Altshuler, B. L.; Khmel'nitzkii, D.; Larkin, A. I.; Lee, P. A. Magnetoresistance and Hall Effect in a Disordered Two-Dimensional Electron Gas. *Phys. Rev. B: Condens. Matter Mater. Phys.* **1980**, *22*, 5142−5153.
(51) Wiegers, G. A. Misfit Layer Compounds: Structures and Physical Properties. *Prog. Solid State Chem.* **1996**, *24*, 1−139.
(52) Bauers, S. R.; Ditto, J.; Moore, D. B.; Johnson, D. C. Structure−property Relationships in Non-Epitaxial Chalcogenide Heterostructures: The Role of Interface Density on Charge Exchange. *Nanoscale* **2016**, *8*, 14665−14672.
(53) Esters, M. Deposition Software for the Inficon IC6 Deposition Controller; https://github.com/marcoesters/deposition_ic6.
(54) Phung, T.; Jensen, J.; Jonshon, D.; Donovan, J.; McBurnett, B. Determination of the Composition of Ultra-Thin Ni-Si Films on Si: Constrained Modeling of Electron Probe Microanalysis and X-ray Reflectivity Data. *X-Ray Spectrom.* **2008**, *37*, 608−614.
(55) Roisnel, T.; Rodríquez-Carvajal, J. WinPLOTR: A Windows Tool for Powder Diffraction Pattern Analysis. *Mater. Sci. Forum* **2001**, *378*−*381*, 118−123.
(56) Rodríguez-Carvajal, J. Recent Advances in Magnetic Structure Determination by Neutron Powder Diffraction. *Phys. B* **1993**, *192*, 55−69.
(57) Schaffer, M.; Schaffer, B.; Ramasse, Q. Sample Preparation for Atomic-Resolution STEM at Low Voltages by FIB. *Ultramicroscopy* **2012**, *114*, 62−71.
(58) Kresse, G.; Hafner, J. *Ab Initio* Molecular-Dynamics Simulation of the Liquid-Metal−Amorphous-Semiconductor Transition in Germanium. *Phys. Rev. B: Condens. Matter Mater. Phys.* **1994**, *49*, 14251−14269.
(59) Kresse, G.; Furthmüller, J. Efficient Iterative Schemes for *Ab Initio* Total-Energy Calculations Using a Plane-Wave Basis Set. *Phys. Rev. B: Condens. Matter Mater. Phys.* **1996**, *54*, 11169−11186.
(60) Kresse, G.; Furthmüller, J. Efficiency of *Ab-Initio* Total Energy Calculations for Metals and Semiconductors Using a Plane-Wave Basis Set. *Comput. Mater. Sci.* **1996**, *6*, 15−50.
(61) Blöchl, P. E. Projector Augmented- Wave Method. *Phys. Rev. B: Condens. Matter Mater. Phys.* **1994**, *50*, 17953−17979.
(62) Kresse, G.; Joubert, D. From Ultrasoft Pseudopotentials to the Projector Augmented-Wave Method. *Phys. Rev. B: Condens. Matter Mater. Phys.* **1999**, *59*, 1758−1775.
(63) Perdew, J. P.; Burke, K.; Ernzerhof, M. Generalized Gradient Approximation Made Simple. *Phys. Rev. Lett.* **1996**, *77*, 3865−3868.
(64) Monkhorst, H. J.; Pack, J. D. Special Points for Brillouin-Zone Integrations. *Phys. Rev. B* **1976**, *13*, 5188−5192.

DOI: 10.1021/acsnano.7b07506
ACS Nano 2018, 12, 1285−1295